

Synthesis of Single Crystals of ϵ -Iron and Direct Measurements of Its Elastic Constants

Agnès Dewaele^{1*}, Bernard Amadon¹, Alexei Bosak², Volodymyr Svitlyk³, and Florent Occelli¹

¹CEA DAM-DIF, F-91297, Arpaçon, France

and Université Paris-Saclay, CEA, Laboratoire Matière en Conditions Extrêmes,
91680 Bruyères-le-Châtel, France

²ESRF, BP220, F-38043 Grenoble Cedex, France

³European Synchrotron Radiation Facility, BP220, 38043 Grenoble Cedex, France
and Helmholtz-Zentrum Dresden-Rossendorf, Institute of Resource Ecology, 01314 Dresden, Germany

 (Received 8 November 2022; accepted 26 April 2023; published 17 July 2023)

Seismology finds that Earth's solid inner core behaves anisotropically. Interpretation of this requires a knowledge of crystalline elastic anisotropy of its constituents—the major phase being most likely ϵ -Fe, stable only under high pressure. Here, single crystals of this phase are synthesized, and its full elasticity tensor is measured between 15 and 33 GPa at 300 K. It is calculated under the same conditions, using the combination of density functional theory and dynamical mean field theory, which describes explicitly electronic correlation effects. The predictive power of this scheme is checked by comparison with measurements; it is then used to evaluate the crystalline anisotropy in ϵ -Fe under higher density. This anisotropy remains of the same amplitude up to densities typical of Earth's inner core.

DOI: 10.1103/PhysRevLett.131.034101

Earth's inner core grows by solidification of the surrounding liquid outer core and is believed to be mainly composed of iron (≥ 90 wt% [1]) alloyed with Ni and lighter elements, likely under a hexagonal-close-packed ϵ -Fe phase unstable under ambient conditions [2,3]. It is anisotropic seismically, with larger compressional P wave velocity v_P for a propagation in the polar rather than the equatorial direction by 3%–4% [4]. Anisotropy in shear waves velocity v_S is estimated to reach 4% [5]. These features are often attributed to a lattice preferred orientation of ϵ -Fe alloy crystallites aligned either during solidification or by deformation. This requires an intrinsic crystalline elastic anisotropy under relevant conditions (330–360 GPa, ~ 5600 K [6]): This anisotropy can be estimated using single-crystal elastic constants (SCECs). SCECs can be straightforwardly measured under pressure using x-ray scattering techniques in single crystals [7], but such a single crystal of ϵ -Fe has never been synthesized. Isotropic or textured powders allowed the measurement of v_P in ϵ -Fe [8–10]. SCECs can also be estimated using lattice strain modeling, but the outputs are highly scattered [9,11,12].

SCECs can be predicted by quantum-mechanics calculations. The standard generalized gradient approximation (GGA) to density functional theory (DFT) provides a reproducible estimate at 0 K and moderate compression for ϵ -Fe [13–17]. However, weaknesses of the DFT/GGA for the description of electron interactions in iron have been pointed out. The density of ϵ -Fe predicted with DFT/GGA is overestimated by more than 5% around 20 GPa [14], and the lattice parameters ratio c/a also differs from the experimental one; SCECs are expected to be highly

sensitive to this ratio [18]. Recent studies suggest that the description of bonding in Fe, and the resulting structural and magnetic properties, can be improved using the combination of DFT and dynamical mean field theory (DMFT) hereafter called DFT + DMFT. DFT + DMFT, unlike DFT alone, allows one to reproduce the loss of magnetism in α -Fe under ambient pressure at Curie temperature, and the α -Fe \rightarrow γ -Fe transformation by a soft phonon mechanism by further temperature increase [19–21]. ϵ -Fe structural parameters are closer to measurements when predicted with DFT + DMFT than with DFT [22,23].

We report here the synthesis of ϵ -Fe single crystals in diamond anvil cells and subsequent measurement of SCECs of this phase up to 32 GPa at 300 K with inelastic x-ray scattering. In parallel, we use the DFT + DMFT description to calculate the SCECs of ϵ -Fe with the finite strain method. We discuss below how they compare and extend DFT + DMFT calculations in the density range of Earth's inner core.

The phase diagram of iron is represented in Fig. 1(f). ϵ -Fe is stable above ~ 13 GPa at 300 K. In earlier studies, α -Fe single crystals have been quasihydrostatically compressed in diamond anvil cells [24,25]; α -Fe \rightarrow ϵ -Fe transformation breaks an α -Fe sample into numerous smaller crystals. This can be explained by the martensitic microstructure observed for this transformation, where ϵ -Fe bursts as many lenticular grains [26]. The lattice and shape mismatches at α -Fe- ϵ -Fe interfaces create a high plastic strain in the sample [25,26], which makes these ϵ -Fe grains unsuitable for fine crystallographic measurements. We show here that ϵ -Fe crystals of

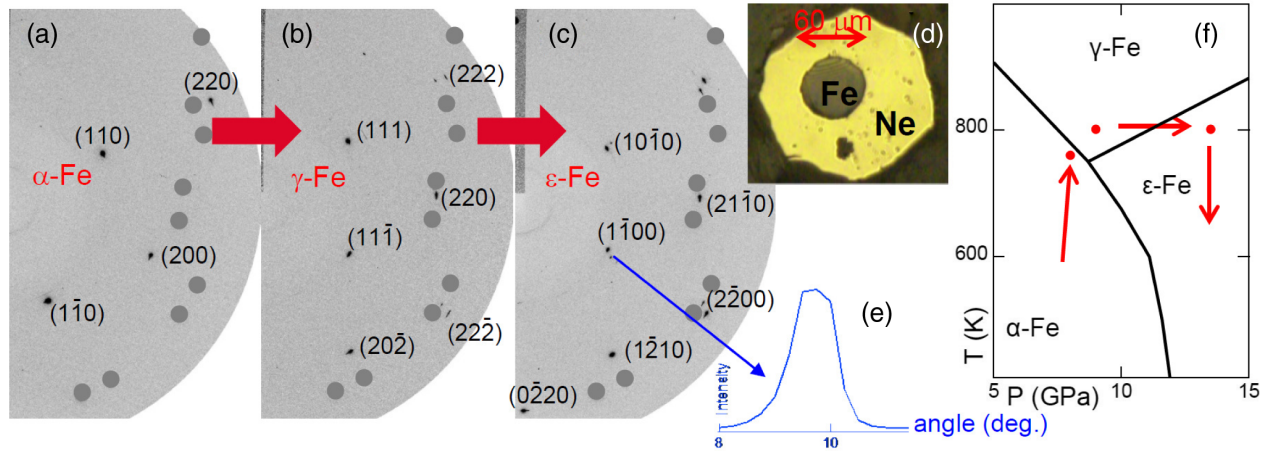


FIG. 1. ϵ -Fe single-crystal synthesis. (a)–(c) X-ray diffraction patterns of an iron sample collected at (a) 8.0 GPa, 770 K, (b) 9.0 GPa, 801 K, and (c) 13.5 GPa, 801 K. The diamond anvil cell has been rotated around a vertical axis by $\pm 20^\circ$ during data collection. (d) Photograph of one sample. (e) Intensity of the (1100) diffraction peak of ϵ -Fe as a function of the diamond anvil cell rotation angle. The rocking curve width is indicative of the crystal quality. (f) Iron phase diagram (after Ref. [24]) showing the approximate P - T path followed for ϵ -Fe single-crystal synthesis. The conditions of the patterns (a)–(c) collection are indicated with red dots.

good quality can be synthesized following an alternative path which rounds the α - γ - ϵ triple point [Fig. 1(f)].

The samples were α -Fe single-crystal samples [$\sim 40 \mu\text{m}$ (diameter) $\times \sim 20 \mu\text{m}$ (thickness)] loaded in neon [Fig. 1(d)]; we monitored their transformations with x-ray diffraction (XRD) mapping in resistively heated diamond anvil cells as detailed in Supplemental Material [27] (which includes Refs. [28–32]). The α -Fe \rightarrow γ -Fe transition was induced by temperature increase to ~ 800 K around 7 GPa; it is obtained within approximately 10 K. Many γ -Fe single crystals formed from one starting α -Fe single crystal, with size reaching 20 μm . Importantly, some crystals were of good quality, as attested by the round shape and narrow rocking curve of the XRD peaks [see Figs. 1(a)–1(c)]. This can be explained by the likely reconstructive character of $\alpha \rightarrow \gamma$ transformation under these conditions [26]. Then, the pressure was increased to induce γ -Fe \rightarrow ϵ -Fe transformation, with no apparent decrease of crystal quality [Fig. 1(c)] and the temperature decreased to 300 K. γ -Fe \rightarrow ϵ -Fe transformation is sluggish, with non-negligible amounts of γ -Fe retained far in the stability field of ϵ -Fe.

Similar P - T paths have been followed for five different samples, but only two of them turned out to contain ϵ -Fe crystals with sufficient size and quality for SCEC measurements. When the size of the starting sample is decreased, the γ -Fe grains size also decreases so that the best syntheses were obtained with the largest samples. In run 1, inelastic x-ray scattering (IXS) measurements have been carried out at 15 GPa; in run 2, at 24 and 33 GPa.

IXS analyzes the signal scattered around single-crystal XRD peaks. Through photon-phonon interaction, a small part of the incident x-ray photons is scattered with an energy decrease or increase ΔE (Stokes or anti-Stokes scattering, creation or annihilation of a phonon) in the

50 meV range for acoustic phonons. The phonon dispersion curves ΔE vs \mathbf{q} (phonon momentum) along several propagation directions have been measured as detailed in Supplemental Material [27] and Refs. [33–35]. This provides acoustic phase velocities of one longitudinal (compressional) wave (v_L) and two transverse waves (v_{T1} and v_{T2}) [36]. Figure 2(a) shows typical IXS spectra collected at 33 GPa. They exhibit an elastic line and two inelastic lines corresponding to one longitudinal and one transverse ($T2$) acoustic phonon energy excited with x rays. The corresponding dispersion curve is plotted in Fig. 2(b).

Hexagonal crystals have five independent SCECs: C_{11} , C_{33} , C_{12} , C_{13} , and the first shear constant C_{44} ; the second shear constant is $C_{66} = (C_{11} - C_{12})/2$. Therefore, five independent velocities have to be measured for a complete determination of the elasticity tensor. For the two samples, eight to 12 dispersion curves allowed a redundant measurement of the five elastic constants from the fit of the dependence of velocities on the propagation direction polar angle [36] (see the expressions of v_L , v_{T1} , v_{T2} in Supplemental Material [27]). The fit results are listed in Table I. Figure 2(c) shows that the velocity data deviate from the fit by $\pm 2\%$ and $\pm 4\%$ for longitudinal and transverse waves, respectively, yielding an estimate of experimental error bars. The uncertainty on C_{11} and C_{33} , deduced from v_L , is thus lower than the uncertainty on C_{44} and C_{66} , deduced from v_{T1} and v_{T2} . The adiabatic bulk modulus of an isotropic aggregate estimated using Voigt averaging of SCECs and using an experimental EOS [37] (with an isothermal-to-adiabatic correction detailed in Sec. 1 of Supplemental Material [27]) are listed in Table I. The two estimates agree within 4% on average, which provides a partial check of the current SCEC measurements. Here, a fast c axis is evidenced for

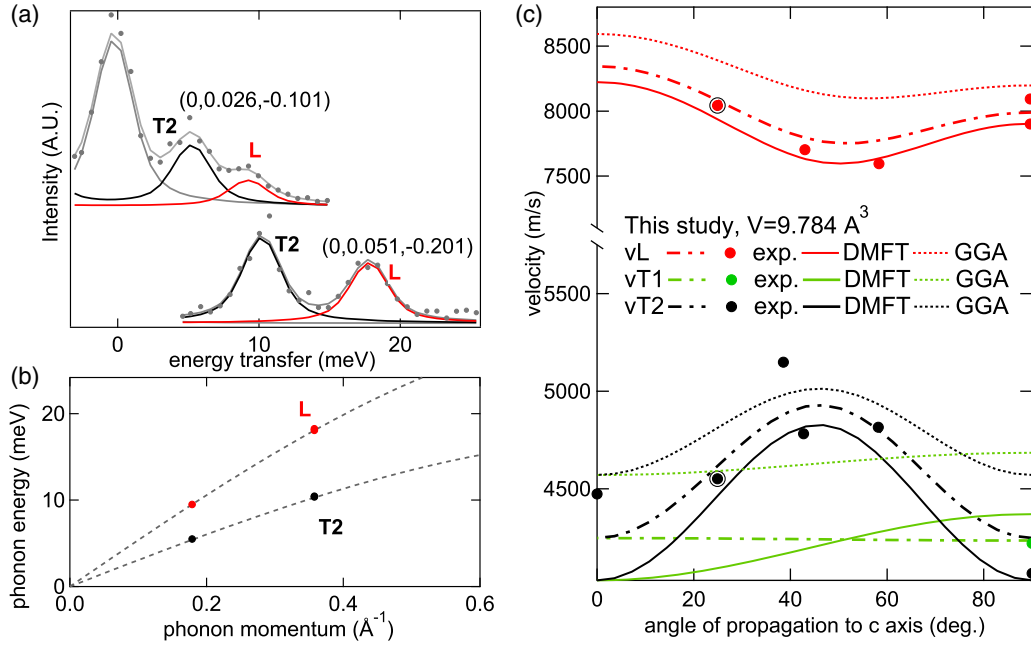


FIG. 2. Measurement of ϵ -Fe single-crystal elastic constants. (a) Inelastic x-ray signal scattered close to an x-ray diffraction spot with $\mathbf{R} = (01\bar{1}\bar{1})$ at 33 GPa. The momentum $\mathbf{q} = \mathbf{Q} - \mathbf{R}$ (see text), indicating the phonon propagation direction, is indicated for each spectrum. One elastic (light gray) and two inelastic (excitation of a transverse $T2$ and longitudinal L phonon in dark gray and red, respectively) contributions fit the raw spectrum. (b) L and $T2$ phonon dispersion curves calculated for a propagation direction parallel to $(01\bar{1}\bar{4})$ using the measurements plotted in (a). (c) Longitudinal and transverse sound velocities, as a function of the propagation direction, measured at 33 GPa (9.75 \AA^3) and calculated at 9.784 \AA^3 (dots, IXS data; rounded dots, IXS data from (b); dot-dashed line, fit to them) are compared to DMFT and DFT/GGA output (continuous and dotted lines).

longitudinal velocity v_L , with a velocity 4.4% higher than in the basal plane. No anisotropy could be detected for v_{T1} , which implies that $C_{44} \simeq C_{66}$. v_{T2} exhibits a 15% increase for a propagation around 50° to the c axis. Similar trends

are observed at 14.5 and 23 GPa (Fig. S2 in the Supplemental Material [27]), but the current anisotropies contrast sharply with IXS measurements on textured powders [9] and those deduced from lattice strain

TABLE I. Comparison of pressure P (in GPa), lattice parameters ratio c/a , single-crystal elastic constants SCECs C_{ij} , and Voigt shear and bulk moduli G and K_S (in GPa) of ϵ -Fe measured and computed in DFT/GGA (“DFT” means “DFT/GGA” in the table) and DFT + DMFT. K_{SEOS} is the bulk modulus deduced from the ϵ -Fe equation of state [37]. Definitions of G , K_S , and K_{SEOS} are in Supplemental Material [27]. Calculations are static; e.g., they do not include a zero-point vibration term. For the DFT + DMFT method, the electronic and lattice temperatures are 300 and 0 K, respectively. Reference [37] is used to evaluate all numbers in parentheses as well as P_{exp} indicated in the footnotes.

Method	V ($\text{\AA}^3/\text{at}$)	P	c/a	C_{11}	C_{33}	C_{66}	C_{13}	C_{44}	G	K_S	K_{SEOS}
Exp.	(10.40)	15	(1.606)	479	495	153	113	142	157	250	(239)
Exp.	(10.05)	24	(1.604)	515	588	147	125	159	169	284	(281)
Exp.	(9.75)	33	(1.602)	605	660	170	171	171	186	343	(322)
DFT	10.450 ^a	-4	1.582	497	548	173	131	159	173	263	264
DFT + DMFT	10.450	11	1.600	453	480	143	116	122	143	243	239
DFT	9.784 ^b	16	1.584	637	700	208	191	198	212	353	355
DFT + DMFT	9.784	30	1.597	592	641	181	174	154	181	331	338
DFT	8.150 ^c	112	1.589	1219	1318	357	452	328	359	730	735
DFT + DMFT	8.150	122	1.597	1164	1281	512	448	318	334	720	721
DFT	6.669 ^d	326	1.594	2281	2508	576	973	538	597	1469	1472
DFT + DMFT	6.669	332	1.598	2241	2452	541	979	556	585	1463	1457

^a $P_{\text{exp}} = 14$ GPa.

^b $P_{\text{exp}} = 32$ GPa.

^c $P_{\text{exp}} = 119$ GPa.

^d $P_{\text{exp}} = 313$ GPa.

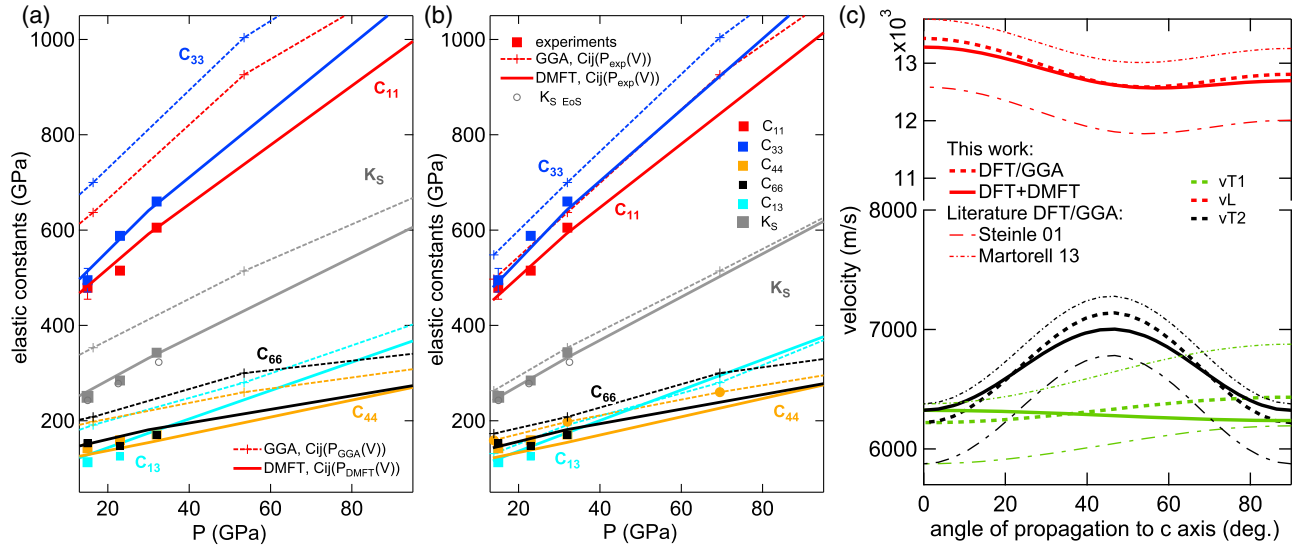


FIG. 3. (a) Calculated single-crystal elastic constants of ϵ -Fe plotted vs pressure $P(V)$ calculated within the same framework. (b) Plotted vs pressure $P_{\text{exp}}(V)$ estimated using an experimental equation of state [37]. Experimental data are represented with colored squares. $K_{S\text{EOS}}$ is from Table I. (c) Predicted acoustic wave anisotropy for ϵ -Fe single crystals around 300 GPa ($6.669 \text{ \AA}^3/\text{at}$) and 0 K. The velocities of the longitudinal and two transverse waves are represented vs the angle of propagation to the hexagonal c axis. Literature predictions at $7.113 \text{ \AA}^3/\text{at}$ [64] and $6.536 \text{ \AA}^3/\text{at}$ [65] are also plotted.

measurements in powders [12] (Fig. S3 in Supplemental Material [27]). A similar disagreement has been reported for cobalt, evidencing the weakness of the underlying stress model [7].

We used DFT + DMFT, which describes explicitly the local electronic interactions among localized $3d$ orbitals [38,39], to predict the ϵ -Fe SCEC. DFT + DMFT modeling requires three main parameters: the choice of correlated $3d$ orbitals, the value of Hubbard U —the effective interaction parameter for direct interaction among d orbitals—and the value of Hund’s J —the effective interaction parameter for exchange interaction [40]. In Supplemental Material [27] (which include Refs. [41–56]), we justify the exchange correlation functional and values of U and J chosen here (local density approximation with $U = 6.0$ eV and $J = 0.9$ eV, close to Ref. [21]). DFT + DMFT predicts ϵ -Fe volume within 1% of the experimental one between 11 and 200 GPa, and a c/a ratio within 0.3% [37,57], a drastic improvement on DFT/GGA (Figs. S4 and S5 in the Supplemental Material [27]).

We have calculated the five independent SCECs at 0 K using the energy finite differences method [13,14,16,17] and five different strains (see Supplemental Material [27], which include Refs. [58–63]), within DFT + DMFT and conventional DFT/GGA at four different ϵ -Fe volumes as listed in Table I, which spans the 11–332 GPa pressure range. DFT + DMFT calculations require a high computing power to ensure an accurate estimation of energy vs strain curves, despite the noise inherent in the Monte Carlo method solving the many-body problem. The pressure, relaxed c/a ratio, and bulk modulus K_S are listed in Table I.

The accuracy of the energy finite differences method has been checked (i) by comparison of finite differences SCECs with density functional perturbation theory SCECs, all obtained with standard DFT (Table S2 in Supplemental Material [27]) and (ii) by comparison of K_S with $K_{S\text{EOS}}$ from the equation of state predicted with the same framework (Table I). In all cases, they agree within 2%.

Figure 3(a) represents the SCECs predicted here vs the calculated pressure as listed in Table I, up to 90 GPa. The SCECs calculated with DFT/GGA agree with Ref. [14] (not plotted here), but are up to 30% higher than the experimental and DFT + DMFT ones. This is in large part because the pressure is underestimated by DFT/GGA; at a fixed pressure, bonding and elastic constants are thus overestimated. This can be corrected by representing SCECs at the same volume rather than the same pressure, as in Fig. 3(b). DFT/GGA, DFT + DMFT, and experimental SCECs then agree within 15%. However, a close look at Fig. 3(b) reveals that while C_{11} , C_{33} , C_{13} , C_{44} , C_{66} are all overestimated by DFT/GGA, by $\sim 10\%$ on average, these constants are closer to experimental values when calculated with DFT + DMFT. This points to a general overestimate of bond strength with DFT. The average deviation of DFT + DMFT C_{ij} from the experimental ones is 4.5%, with a maximum for C_{44} , underestimated by $\sim 12\%$; this results in a difference of 3.5% in v_{T1} anisotropy. This difference may be partly explained by experimental error bars. Measured and calculated acoustic velocity anisotropies exhibit similar shapes [Fig. 2(c)]. DFT + DMFT thus improves the description of elastic behavior of ϵ -Fe under pressure compared to DFT. Elastic constants being second

derivatives of energy are a stringent test of the modeling. The validation of the DFT + DMFT predictions under moderate compression enables us to use it with some confidence in a domain where SCEC measurements are not available yet, e.g., around 330–360 GPa, the pressure of Earth’s inner core.

Figure 3(c) represents the longitudinal and transverse acoustic velocities predicted with DFT + DMFT, as well as DFT/GGA for an ϵ -Fe volume of $6.669 \text{ \AA}^3/\text{at}$, as a function of the propagation direction. The difference between DFT/GGA and DFT + DMFT modeling diminishes as compression increases, because the electronic correlation effects decrease when the electronic bandwidth increases. At $6.669 \text{ \AA}^3/\text{at}$, predicted P , c/a , and SCECs are close for the two frameworks (Table I), and the anisotropy trends are similar. Some earlier DFT/GGA predictions provide similar shapes for v_L and v_{T2} [64,65]; the predictions made by another group differ [16,17]. v_{T1} trends are more scattered, which suggests weaker constraints on C_{44} and C_{66} than C_{11} and C_{33} . The majority of *ab initio* simulations predicts that around 300–350 GPa and 0 K, c axis of ϵ -Fe single crystals is fast for v_L (by $\sim 6\%$), regardless of the modeling of electronic correlations. Temperature effects need to be taken into account to predict v_L anisotropy in Earth’s inner core; this has been done by straining an *ab initio* molecular dynamics box [65]. A temperature increase to 5500 K is found to increase v_L anisotropy by 2%. Other simulation techniques should be used to confirm this [66].

To sum up, in this work, we have taken advantage of the different mechanisms of solid-solid phase transformations in iron to control the microstructure of samples and obtain single crystals of the high-pressure ϵ -Fe phase through the $\alpha \rightarrow \gamma \rightarrow \epsilon$ path. Then, direct measurements of ϵ -Fe single crystal elastic constants have been performed up to 32 GPa. We have found that the c axis is 4.4% faster for v_p . In parallel, a state-of-the-art technique for the modeling of bonding in correlated electronic systems has been used to predict these elastic constants. They agree with the measured ones, which validates this description and places dense iron *ab initio* modeling on firm footing. The crystalline elastic anisotropy of ϵ -Fe is predicted to persist up to the densities of Earth’s inner core.

We acknowledge synchrotron ESRF for the provision of beamtime under Proposals No. HC-3945, No. HC-3402, No. HC-3104, and No. HC-2783. We thank Mohamed Mezouar and Paul Loubeyre for discussions and support, Yves-Patrick Pellegrini for his help with elastic constants calculation, and Leonid Pourovskii for discussions on DMFT. We acknowledge numerous helpful discussions and data sharing with Johann Bouchet and François Bottin. We thank Jeroen Jacobs for his help with ESRF vacuum heater.

*agnes.dewaele@cea.fr

- [1] D. Alfè, M. J. Gillan, and G. D. Price, *Nature (London)* **405**, 172 (2000).
- [2] F. Coppari, D. E. Fratanduono, M. Millot, R. G. Kraus, A. Lazicki, J. R. Rygg, R. F. Smith, and J. H. Eggert, *Phys. Rev. B* **106**, 134105 (2022).
- [3] S. Tateno, K. Hirose, Y. Ohishi, and Y. Tatsumi, *Science* **330**, 359 (2010).
- [4] A. Deuss, *Annu. Rev. Earth Planet. Sci.* **42**, 103 (2014).
- [5] B. G. Delbridge and M. Ishii, *Geophys. J. Int.* **222**, 1135 (2020).
- [6] S. Anzellini, A. Dewaele, M. Mezouar, P. Loubeyre, and G. Morard, *Science* **340**, 464 (2013).
- [7] D. Antonangeli, S. Merkel, and D. L. Farber, *Geophys. Res. Lett.* **33**, L24303 (2006).
- [8] G. Fiquet, J. Badro, F. Guyot, H. Requardt, and M. Krisch, *Science* **291**, 468 (2001).
- [9] W. L. Mao, V. V. Struzhkin, A. Q. R. Baron, S. Tsutsui, C. E. Tommaseo, H.-R. Wenk, M. Y. Hu, P. Chow, W. Sturhahn, J. Shu, R. J. Hemley, D. L. Heinz, and H.-K. Mao, *J. Geophys. Res.* **113**, B09213 (2008).
- [10] A. E. Gleason, W. L. Mao, and J. Y. Zhao, *Geophys. Res. Lett.* **40**, 2983 (2013).
- [11] A. K. Singh, H.-K. Mao, J. Shu, and R. J. Hemley, *Phys. Rev. Lett.* **80**, 2157 (1998).
- [12] S. Merkel, J. Shu, P. Gillet, H. Mao, and R. Hemley, *J. Geophys. Res.* **110**, B05201 (2005).
- [13] L. Stixrude and R. E. Cohen, *Science* **267**, 1972 (1995).
- [14] G. Steinle-Neumann, L. Stixrude, and R. E. Cohen, *Phys. Rev. B* **60**, 791 (1999).
- [15] L. Vocadlo, D. P. Dobson, and I. G. Wood, *Earth Planet. Sci. Lett.* **288**, 534 (2009).
- [16] X. Sha and R. E. Cohen, *Phys. Rev. B* **81**, 094105 (2010).
- [17] X. Sha and R. E. Cohen, *Geophys. Res. Lett.* **37**, L10302 (2010).
- [18] C. Gannarelli, D. Alfe, and M. Gillan, *Phys. Earth Planet. Inter.* **152**, 67 (2005).
- [19] I. Leonov, A. I. Poteryaev, V. I. Anisimov, and D. Vollhardt, *Phys. Rev. Lett.* **106**, 106405 (2011).
- [20] I. Leonov, *Sci. Rep.* **4**, 5585 (2014).
- [21] Q. Han, T. Biroli, and K. Haule, *Phys. Rev. Lett.* **120**, 187203 (2018).
- [22] K. Glazyrin, L. V. Pourovskii, L. Dubrovinsky, O. Narygina, C. McCammon, B. Hewener, V. Schünemann, J. Wolny, K. Muffler, A. I. Chumakov, W. Crichton, M. Hanfland, V. B. Prakapenka, F. Tasnadi, M. Ekholm, M. Aichhorn, V. Vildosola, A. V. Ruban, M. I. Katsnelson, and I. A. Abrikosov, *Phys. Rev. Lett.* **110**, 117206 (2013).
- [23] L. V. Pourovskii, J. Mravlje, M. Ferrero, O. Parcollet, and I. A. Abrikosov, *Phys. Rev. B* **90**, 155120 (2014).
- [24] A. Dewaele, V. Svitlyk, F. Bottin, J. Bouchet, and J. Jacobs, *Appl. Phys. Lett.* **112**, 201906 (2018).
- [25] A. Dewaele, C. Denoual, S. Anzellini, F. Occelli, M. Mezouar, P. Cordier, S. Merkel, M. Véron, and E. Rausch, *Phys. Rev. B* **91**, 174105 (2015).
- [26] E. Boulard, C. Denoual, A. Dewaele, A. King, Y. Le Godec, and N. Guignot, *Acta Mater.* **192**, 30 (2020).
- [27] See Supplemental Material at <http://link.aps.org/supplemental/10.1103/PhysRevLett.131.034101> for experimental methods and theoretical methods.

- [28] D. L. Farber, D. Antonangeli, C. M. Aracne, and J. Benterou, *High Press. Res.* **26**, 1 (2006).
- [29] F. Datchi, R. LeToullec, and P. Loubeyre, *J. Appl. Phys.* **81**, 3333 (1997).
- [30] R. G. Burkovsky, I. Bronwald, D. Andronikova, B. Wehinger, M. Krisch, J. Jacobs, D. Gambetti, K. Roleder, A. Majchrowski, A. V. Filimonov, A. I. Rudskoy, S. B. Vakhrushev, and A. K. Tagantsev, *Sci. Rep.* **7**, 41512 (2017).
- [31] A. Hammersley, FIT2D: An introduction and overview, ESRF Technical Report No. ESRF97HA02, 1997.
- [32] C. Prescher and V. B. Prakapenka, *High Press. Res.* **35**, 223 (2015).
- [33] M. Krisch and F. Sette, in *Light Scattering in Solids IX: Novel Materials and Techniques*, Topics in Applied Physics Vol. 108, edited by M. Cardona and R. Merlin (Springer International Publishing Ag., 2007), pp. 317–369.
- [34] F. Occelli, M. Krisch, P. Loubeyre, F. Sette, R. LeToullec, C. Masciovecchio, and J.-P. Rueff, *Phys. Rev. B* **63**, 224306 (2001).
- [35] B. Wehinger, A. Bosak, S. Nazzareni, D. Antonangeli, A. Mirone, S. L. Chaplot, R. Mittal, E. Ohtani, A. Shatskiy, S. Saxena, S. Ghose, and M. Krisch, *Geophys. Res. Lett.* **43**, 2568 (2016).
- [36] M. J. P. Musgrave, *Crystal Acoustics* (Holden Days, San Francisco, 1970).
- [37] A. Dewaele, P. Loubeyre, F. Occelli, M. Mezouar, P. I. Dorogokupets, and M. Torrent, *Phys. Rev. Lett.* **97**, 215504 (2006).
- [38] A. Georges, G. Kotliar, W. Krauth, and M. J. Rozenberg, *Rev. Mod. Phys.* **68**, 13 (1996).
- [39] G. Kotliar, S. Y. Savrasov, K. Haule, V. S. Oudovenko, O. Parcollet, and C. A. Marianetti, *Rev. Mod. Phys.* **78**, 865 (2006).
- [40] V. I. Anisimov and O. Gunnarsson, *Phys. Rev. B* **43**, 7570 (1991).
- [41] B. Amadon, *J. Phys. Condens. Matter* **24**, 075604 (2012).
- [42] J. Bieder and B. Amadon, *Phys. Rev. B* **89**, 195132 (2014).
- [43] X. Gonze *et al.*, *Comput. Phys. Commun.* **205**, 106 (2016).
- [44] X. Gonze *et al.*, *Comput. Phys. Commun.* **248**, 107042 (2020).
- [45] A. H. Romero *et al.*, *J. Chem. Phys.* **152**, 124102 (2020).
- [46] B. Amadon, F. Lechermann, A. Georges, F. Jollet, T. O. Wehling, and A. I. Lichtenstein, *Phys. Rev. B* **77**, 205112 (2008).
- [47] B. Amadon, *Phys. Rev. B* **94**, 115148 (2016).
- [48] H. Chen and A. J. Millis, *Phys. Rev. B* **93**, 045133 (2016).
- [49] F. Gendron, N. Cliche, and B. Amadon, *J. Phys. Condens. Matter* **34**, 464003 (2022).
- [50] A. S. Belozero, A. A. Katanin, V. Y. Irkhin, and V. I. Anisimov, *Phys. Rev. B* **101**, 155126 (2020).
- [51] J. M. Tomczak, T. Miyake, R. Sakuma, and F. Aryasetiawan, *Phys. Rev. B* **79**, 235133 (2009).
- [52] S. K. Panda, H. Jiang, and S. Biermann, *Phys. Rev. B* **96**, 045137 (2017).
- [53] B. Amadon, T. Applencourt, and F. Bruneval, *Phys. Rev. B* **89**, 125110 (2014).
- [54] J.-B. Morée and B. Amadon, *Phys. Rev. B* **98**, 205101 (2018).
- [55] A. Dewaele and L. Nataf, *Phys. Rev. B* **106**, 014104 (2022).
- [56] Q. Wei, C. McCammon, and S. A. Gilder, *Geochem. Geophys. Geosyst.* **18**, 4646 (2017).
- [57] A. Dewaele and G. Garbarino, *Appl. Phys. Lett.* **111**, 021903 (2017).
- [58] R. A. Johnson, *Model. Simul. Mater. Sci. Eng.* **1**, 717 (1993).
- [59] G. Steinle-Neumann and R. E. Cohen, *J. Phys. Condens. Matter* **16**, 8783 (2004).
- [60] T. H. K. Barron and M. L. Klein, *Proc. Phys. Soc. London* **85**, 523 (1965).
- [61] G. V. Sin'ko, *Phys. Rev. B* **77**, 104118 (2008).
- [62] D. R. Hamann, X. Wu, K. M. Rabe, and D. Vanderbilt, *Phys. Rev. B* **71**, 035117 (2005).
- [63] A. Martin, M. Torrent, and R. Caracas, *Phys. Rev. B* **99**, 094112 (2019).
- [64] G. Steinle-Neumann, L. Stixrude, R. Cohen, and O. Gulseren, *Nature (London)* **413**, 57 (2001).
- [65] B. Martorell, J. Brodholt, I. G. Wood, and L. Vocadlo, *Earth Planet. Sci. Lett.* **365**, 143 (2013).
- [66] J. Bouchet, F. Bottin, D. Antonangeli, and G. Morard, *J. Phys. Condens. Matter* **34**, 344002 (2022).